NANO LETTERS

pubs.acs.org/NanoLett Letter

Excitations of Intercalated Metal Monolayers in Transition Metal Dichalcogenides

Shiyu Fan, Sabine Neal, Choongjae Won, Jaewook Kim, Deepak Sapkota, Feiting Huang, Junjie Yang, David G. Mandrus, Sang-Wook Cheong, Jason T. Haraldsen, and Janice L. Musfeldt*

Cite This: *Nano Lett.* 2021, 21, 99–106 Read Online

ACCESS | Metrics & More | Article Recommendations | Supporting Information

ABSTRACT: We combine Raman scattering spectroscopy and lattice dynamics calculations to reveal the fundamental excitations of the intercalated metal monolayers in the Fe_xTaS_2 (x = 1/4, 1/3) family of materials. Both in- and out-of-plane modes are identified, each of which has trends that depend upon the metal−metal distance, the size of the van der Waals gap, and the metal-to-chalcogenide slab mass ratio. We test these trends against the response of similar systems, including Cr-intercalated NbS_2 and $RbFe(SO_4)_2$, and demonstrate that the metal monolayer excitations are both coherent and tunable. We discuss the consequences of intercalated metal monolayer excitations for material properties and developing applications.

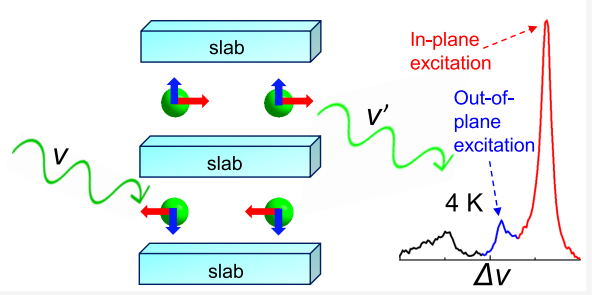

KEYWORDS: *intercalated transition metal dichalcogenides, excitations of intercalated metal monolayers, structure−property relations involving metal monolayer excitations*

INTRODUCTION

Metal monolayers have a long and fascinating history.[1] Whether due to surface adsorption[2,3] or intercalation,[4] these structures display distinctive electronic and magnetic properties[5,6] and play key roles in photovoltaic cells,[7] semiconductor surfaces,[8] and catalysts for batteries.[9] The importance of monolayer interactions has been demonstrated in metal intercalated graphite[10−12] and bilayer graphene,[13,14] both of which reveal superconductivity. Metal centers can also be intercalated into other van der Waals materials such as transition metal dichalcogenides,[5,15,16] forming different patterns within the gap depending upon the concentration. When incorporated in this manner, metal monolayers support high temperature magnetic ordering,[17−19] novel metallicity that is distinct from that of the parent compound,[20,21] and superconductivity.[22−24] Intercalated metal monolayers are also responsible for the development of different types of domain walls in layered chalcogenides.[25] The Fe_xTaS_2 family of materials[25] attracted our attention as a platform with which to reveal the fundamental excitations of the atomically-thin network of metal atoms embedded within the van der Waals gap.

2H-TaS_2 is well-known to display a $P6_3/mmc$ space group.[26] The crystal structure consists of TaS_2 slabs separated by a van der Waals gap and stacked together along the c-axes. Within a slab, each Ta center is surrounded by a trigonal prism of S anions. The structures of Fe_xTaS_2 (x = 1/4 and 1/3) are shown in Figure 1a,b. It is well-established that the transition metal dichalcogenide layers have strong covalent bonding, leaving the Fe atoms (which form a single metallic layer within the van der Waals gap) weakly bound. We refer to these ultrathin well-ordered metal layers as "monolayers" or "atomically thin layers of metal atoms sandwiched between chalcogenide slabs", but of course, they are not isolated, free-standing monolayers in the sense of graphene or other exfoliated systems. They are embedded in the crystal itself: a consequence of the intercalation process. As shown in Figure 1a,b, the x = 1/4 system is centrosymmetric, whereas the x = 1/3 material is non-centrosymmetric and chiral.[25] The embedded Fe monolayer brings a significant, distinct density of states to the Fermi level[29−31] and a narrow free-carrier response to the optical properties (in addition to the Drude that emanates from 2H-TaS_2 itself).[20] Chirality in the x = 1/3 member manifests in (i) the nature of the hole/electron pockets, (ii) electron density patterns in the Fe plane, and (iii) the formation of $Z_2 \times Z_3$ structural domains with Z_6 vortices.[20,25]

The entire family of Fe_xTaS_2 materials is metallic. As demonstrated by prior optical properties work,[20] metallic character precludes observation of odd-symmetry infrared-active phonons across the various magnetic transitions due to

Received: August 15, 2020
Revised: November 10, 2020
Published: December 2, 2020

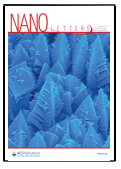

https://dx.doi.org/10.1021/acs.nanolett.0c03292
Nano Lett. 2021, 21, 99−106

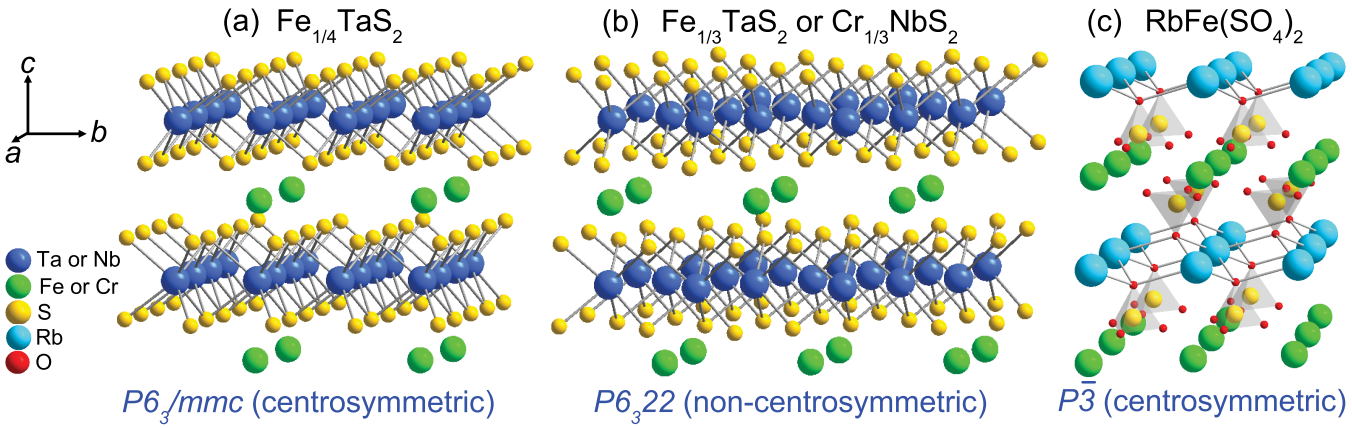

Figure 1. (a) $Fe_{1/4}TaS_2$ displays a centrosymmetric $P6_3/mmc$ space group.[25] The Fe layers have a $2a \times 2a$ superstructure in the plane and an AA-type stacking pattern along the *c*-axis. (b) Non-centrosymmetric, chiral structure of $Fe_{1/3}TaS_2$ and $Cr_{1/3}NbS_2$ (space group $P6_322$).[25,27] The Fe layers have a $\sqrt{3}a \times \sqrt{3}a$ superstructure in the plane and an AB-type stacking pattern along *c*. (c) Crystal structure of $RbFe(SO_4)_2$ at room temperature (space group $P\bar{3}$).[28] This system also has an Fe monolayer with AA-type stacking.

screening by the free carrier response. As a result, the local lattice distortions in this class of materials, particularly those that involve the metal monolayer, are highly underexplored. This is problematic because, as we discuss below, a number of properties and mechanisms depend upon phonons and their behavior.[32] We therefore turn to Raman scattering spectroscopy to reveal the even-symmetry vibrational modes and to search for evidence of metal monolayer excitations. As a reminder, the selection rules of infrared and Raman scattering spectroscopies determine whether odd or even symmetry vibrational modes are sampled. It is the site-specific nature of these techniques that allows us to extract the signature of the metal monolayer from the complex mode pattern in these materials.

To explore the vibrational properties of intercalated chalcogenides, we measured the Raman response of Fe_xTaS_2 (x = 0, 1/4, and 1/3) and compare our findings with complementary lattice dynamics calculations. For the first time, we identify a set of characteristic excitations of the embedded Fe monolayer that have both in- and out-of-plane components. These in- and out-of-plane vibrations of the intercalated Fe monolayer reveal frequency, line width, and intensity trends as well as spin-phonon coupling. To test whether similar excitations appear in other systems with weakly bound layers, we extend our work to include Cr_xNbS_2 (x = 0, 1/3)[18,33−37] and $RbFe(SO_4)_2$[28,38,39] which have comparable metal ordering patterns inside the van der Waals gap (Figure 1b,c). In each case, we find that the metal monolayer is moving in a coherent fashion, not just filling space, adding/subtracting, or compensating charge. These results enable the development of structure−property relations and modeling of frequency vs mass ratio effects. We discuss the consequences of in- and out-of-plane metal monolayer excitations on the properties of these materials as well.

RESULTS AND DISCUSSION

Localized Vibrational Modes Induced by Fe Intercalation. Figure 2a displays the Raman spectra of the Fe_xTaS_2 family of materials at room temperature. We begin by assigning the modes of the parent compound, a process that also isolates excitations that emanate from the intercalated metal layer. In line with prior work on 2H-TaS_2, we assign peaks at 240, 308, and 380 cm^{-1} as E_{1g}, E_{2g}, and A_{1g} modes, respectively (Table S1).[40−44] We do not observe the 26 cm^{-1} E_{2g} mode due to the use of a cut-off filter. We assign the broad band centered near 180 cm^{-1} as a two-phonon mode.[41,44,45] It arises from the persistence of short-range charge density waves[44] and diminishes at low temperatures due to screening (Figure S2a). Several other features below 110 cm^{-1} are activated by remnant charge density wave effects as well.[43,44] A detailed analysis of the temperature trends is available in the Supporting information.

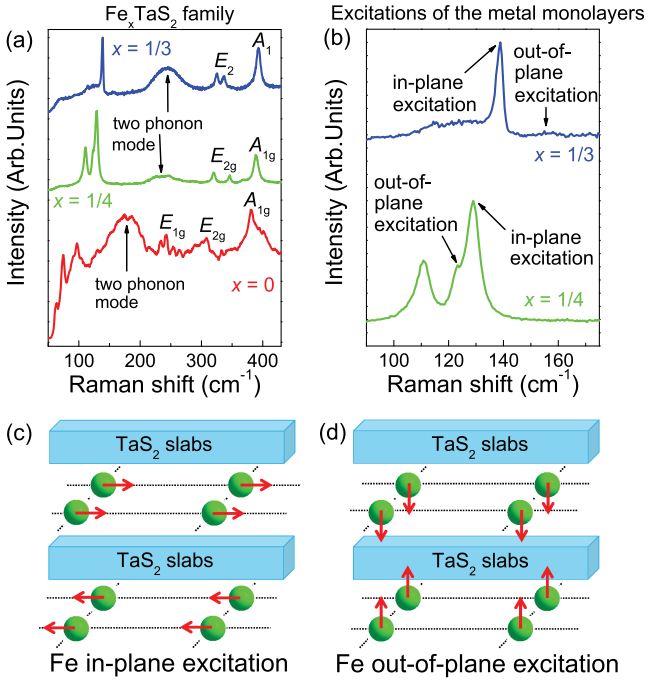

Figure 2. (a) Raman spectra of the Fe_xTaS_2 family of materials (x = 0, 1/4, and 1/3) at 300 K. (b) Close-up view of the in- and out-of-plane Fe monolayer excitations in $Fe_{1/4}TaS_2$ and $Fe_{1/3}TaS_2$. (c,d) Schematic view of the in- and out-of-plane excitations of the Fe monolayer. Animated .gif files are available in the Supporting Information.

Next, we turn our attention to the intercalated materials (Figure 2a). A similar mode pattern emanates from the transition metal dichalcogenide slabs in the x = 1/4 and 1/3 compounds, although the exact symmetry designations reflect space group differences (Figure 1). The response below 200

https://dx.doi.org/10.1021/acs.nanolett.0c03292
Nano Lett. 2021, 21, 99−106

cm^{-1} is more interesting. In the $x = 1/4$ compound, peaks emerge at 122 and 129 cm^{-1}, whereas in the $x = 1/3$ material, new features appear at 139 and 156 cm^{-1} (Figure 2b). These structures are not observed in the parent compound. Based upon our lattice dynamics calculations, we assign these peaks as in- and out-of-plane excitations of the Fe monolayer. The 156 cm^{-1} out-of-plane excitation in the $x = 1/3$ material is weak - consistent with predictions for a small matrix element, although it is easier to see at low temperature (Figure S7a). The frequency separation between the in- and out-of-plane modes of the intercalated metal monolayer is nicely predicted by our first-principles calculations as well (Figure S8). We therefore find that an intercalated metal monolayer has a unique set of excitations and a fully-identifiable pattern even though it resides inside the van der Waals gap of a more complex material. The exact displacement pattern is challenging to visualize, but the motion is similar to that shown in the schematics (Figure 2c,d). Animated gif files showing the full complexity of these vibrational modes in both $Fe_{1/4}TaS_2$ and $Fe_{1/3}TaS_2$ are available in Supporting Information.

Figure 2b displays a close-up view of the Fe monolayer excitations. A chalcogenide layer twisting mode involving weak interlayer interactions between the monolayer and TaS_2 slab is observed near 110 cm^{-1} as well. Although the in- and out-of-plane metal monolayer excitations have similar frequencies, they are best distinguished by relative intensities. The in-plane excitation is always the most intense. To understand why this is so, it is important to realize that the TaS_2 slabs are not rigid. As a result, they interact with (and dampen) the out-of-plane excitations of the metal monolayer. This effect is especially important in the $x = 1/4$ material and even causes the frequency of the out-of-plane excitation to shift below that of the in-plane mode. By contrast, in-plane Fe monolayer excitation is relatively unencumbered by the TaS_2 slabs. This leads to a higher intensity for the in-plane mode and a weaker intensity for the out-of-plane counterpart. The out-of-plane excitation is easy to identify in $Fe_{1/4}TaS_2$, but it is extremely weak in $Fe_{1/3}TaS_2$. We discuss frequency trends below.

Metal Monolayer Excitations in Related Materials. To develop structure−property relations involving intercalated metal monolayer excitations, we extended these Raman scattering measurements to include several related compounds. We begin with Cr_xNbS_2 ($x = 0$ and $1/3$) due to the similarity in the crystal structure and packing pattern of the Cr monolayer. Another reason for this selection is that 2H-NbS_2 does not have any charge density wave transitions,[46−49] so no new peaks emerge due to low-temperature symmetry breaking (Figure S2c). Figure 3a displays the Raman spectra of the Cr_xNbS_2 family of materials ($x = 0$ and $1/3$). As expected, E_{1g}, E_{2g}, and A_{1g} modes are observed in the 2H-parent compound. The two-phonon mode is absent due to the lack of a density wave ground state. Turning to the $x = 1/3$ system, in- and out-of-plane vibrational modes of the Cr network are identified at 192 and 208 cm^{-1}, respectively. As before, the in-plane excitation is most intense. The out-of-plane excitation is significantly less intense compared to the in-plane mode, and it resonates at a higher frequency. This is because, although the out-of-plane excitation contains a small amount of slab motion, it is a less important part of the displacement pattern in the $x = 1/3$ system (compared to $x = 1/4$). We therefore see that metal monolayer excitations are an intrinsic part of the dynamics of intercalated transition metal dichalcogenides.

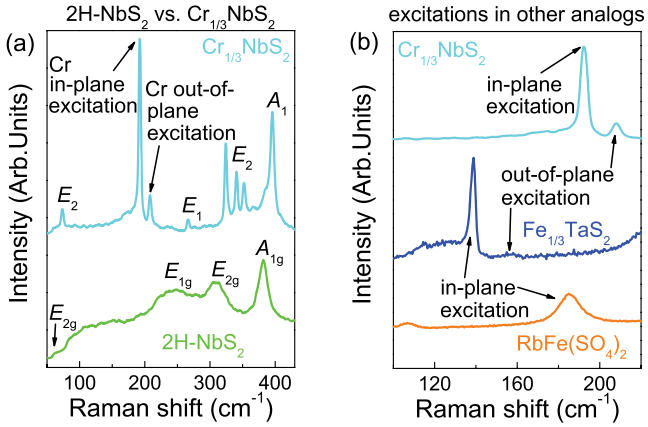

Figure 3. (a) Raman scattering spectra of the Cr_xNbS_2 family of materials ($x = 0$ and $1/3$) at 300 K. (b) A close-up view of the in- and out-of-plane metal monolayer modes in $Cr_{1/3}NbS_2$, $Fe_{1/3}TaS_2$, and $RbFe(SO_4)_2$.

To further test our findings, we measured the Raman scattering response of $RbFe(SO_4)_2$. This system has Fe monolayers sandwiched between $Rb(SO_4)_2$ slabs with an AA-type stacking along the c-axis (Figure 1c). Figure 3b displays a close-up view of the Raman spectrum of $Cr_{1/3}NbS_2$, $Fe_{1/3}TaS_2$, and $RbFe(SO_4)_2$. Well-defined metal monolayer excitations emerge in all three compounds. The out-of-plane Fe monolayer mode is not present in $RbFe(SO_4)_2$ - even though the in-plane component is strong. We attribute its disappearance to the extremely narrow 2.31 Å van der Waals gap in this system[28] (Table 1), which quenches the out-of-plane motion of the embedded Fe monolayer.

Table 1. Summary of in-Plane Metal−Metal Distances, Thicknesses of Van Der Waals Gaps, and Mass Ratios for the Materials of Interest[a]

materials	in-plane metal−metal distance (Å)	thickness of van der Waals gap (Å)	mass ratio
$Fe_{1/4}TaS_2$	6.61	2.93	0.06
$Fe_{1/3}TaS_2$	5.73	3.07	0.08
$Cr_{1/3}NbS_2$	5.75	2.89	0.11
$RbFe(SO_4)_2$	4.71	2.31	0.20

[a]The metal−metal distances and van der Waals gap thicknesses are extracted from their structure files.[19,30,38] The mass ratio is defined as $c \times M_{interc}/M_{host}$. Here, c is the concentration of intercalated element, M_{interc} is the atomic mass of the intercalated element, and M_{host} is the atomic mass of the host elements.

Figure 4 summarizes how the monolayer excitations scale with characteristic distances and the metal-to-chalcogenide slab mass ratio. These parameters are summarized in Table 1. We find that the frequencies of the in- and out-of-plane metal monolayer excitations decrease with increasing metal−metal distance in the plane (Figure 4a,b). These trends emanate from softer potentials (and weaker force constants) in more weakly associated lower concentration networks. As we shall see below, an analysis of frequency trends in terms of the mass ratio provides an even more comprehensive framework for understanding these effects.

The in-plane metal−metal distance also impacts relative intensities of monolayer excitations (Figure 4c). The intensity of the out-of-plane excitation diminishes (and even falls to zero in $RbFe(SO_4)_2$) as the Fe network tightens and the narrower

https://dx.doi.org/10.1021/acs.nanolett.0c03292
Nano Lett. 2021, 21, 99−106

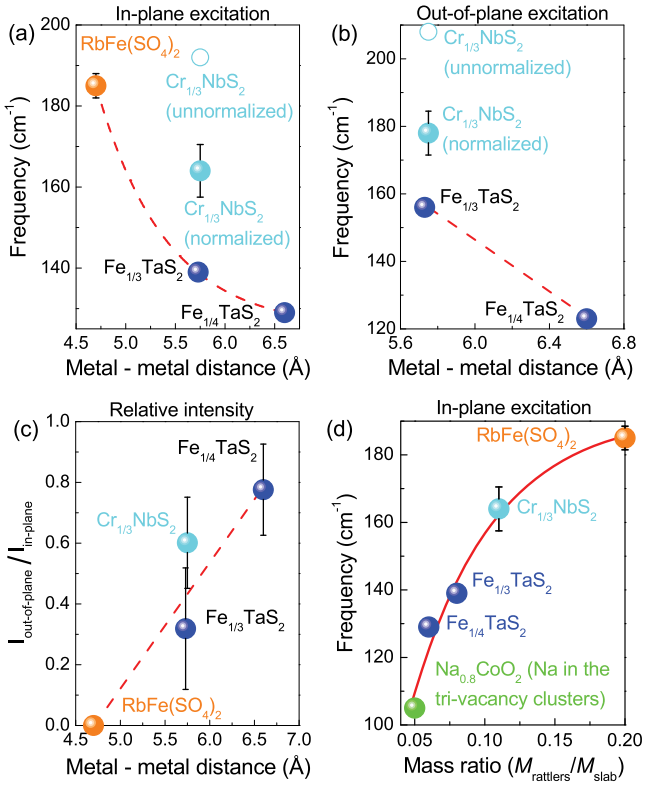

Figure 4. (a) Frequency of the in-plane metal monolayer excitation vs in-plane metal−metal distance in Fe_xTaS_2 (x = 1/4 and 1/3) and the analog materials. Results from $Cr_{1/3}NbS_2$ are normalized by the mass of the transition metal center as well as the slabs to better compare with the Fe-containing series. (b) Out-of-plane monolayer excitations as a function of in-plane metal−metal distance. (c) Relative intensity of the out-of-plane to in-plane rattling mode vs in-plane metal−metal distance. (d) In-plane frequency vs mass ratio between the intercalated metal monolayer and the chalcogenide slab. The red line is a fit to eq 2. We find $\omega_{R,max}$ = 192 cm^{-1} and κ = 0.059.

van der Waals gap confines motion to the *ab*-plane. In other words, when tightly packed, the out-of-plane motion of the metal monolayer is quenched because the matrix element drops to zero.

Modeling Frequency vs Mass Ratio Effects. To examine the frequency vs mass ratio relationship, we expanded the mode frequency ω_m about the mass ratio μ as

$$\omega_m = \omega_{m,max} - \kappa(d\omega_m/d\mu) \quad (1)$$

Here, $\omega_{m,max}$ is the maximum mode frequency, and κ is an "effective" spring ratio between the monolayer and slab. The mass ratio is defined as the ratio of metal monolayer to the slab within the unit cell (M_m/M_s) (Table 1). For example, the metal to chalcogenide slab mass ratio for $Fe_{1/4}TaS_2$ is calculated as mass ratio = $1/4M_{Fe}/(M_{Ta} + 2M_S)$ = $0.25 \times 56/(181 + 2 \times 32)$ = 0.06. Assuming that κ is constant for the mode environment, frequency is given by

$$\omega_m = \omega_{m,max}(1 - e^{-\mu/\kappa}) \quad (2)$$

This solution fits the data in Figure 4d very well. We extract a maximum in-plane mode frequency of 192 cm^{-1} and an effective spring ratio of 0.059 for our materials. Eq 2 also has a conceptually interesting limit impacting the growth process of these materials. Comparing the maximum mode frequency to the data in Figure 4a, we find that the minimum metal−metal distance is near 4.5 Å. The maximum possible mass ratio is therefore between 0.21 and 0.25, suggesting an intercalation threshold. Beyond this limit, interlayer interactions become comparable to intralayer interactions, blurring the distinction between weakly bound metal monolayers between chalcogenide slabs and a more standard multilayered material.

Initially, only the Fe and Cr systems were used for the fit, providing a prediction for other similar materials. To test our model further, we included data from ref 50. In sodium intercalated cobalt dioxide ($Na_{0.8}CoO_2$), only the Na atoms in the 2b Wyckoff site associated with clusters of three vacancies display in-plane excitations.[50] Strikingly, the mode frequency of $Na_{0.8}CoO_2$ is in excellent agreement with the overall frequency vs mass ratio trend (Figure 4d). The agreement reveals that, for this specific type of chemical and interaction environment, the mass ratio effect is general. Different chemical and interaction environments, however, modify the effective spring ratio for an intercalated metal monolayer. This effect is illustrated in Figure S5f where different $\omega_{m,max}$ and κ parameters are required to capture out-of-plane mode frequency vs mass ratio effects for the same set of materials. That the spring constant ratio is different for in- vs out-of-plane fits makes sense because the layer/slab interactions are distinct. Further discussion of the mass ratio is available in Supporting Information.

Spin-Phonon Coupling in $Fe_{1/4}TaS_2$. To further explore metal monolayer excitations, we measured the Raman response

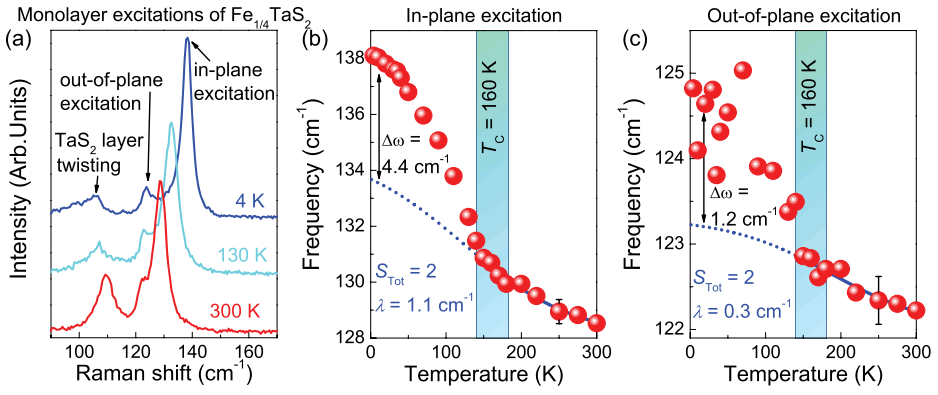

Figure 5. (a) Close-up view of the Raman response of $Fe_{1/4}TaS_2$ as a function of temperature. (b) In-plane mode frequency of the Fe monolayer vs temperature. (c) Frequency of the out-of-plane mode of the Fe monolayer vs temperature.

https://dx.doi.org/10.1021/acs.nanolett.0c03292
Nano Lett. 2021, 21, 99−106

of these materials as a function of temperature. $Fe_{1/4}TaS_2$ is unique in that it exhibits strong spin-phonon coupling across the magnetic ordering transition. This coupling may be due to the robust ferromagnetic ground state and sharp coercive field in the $x = 1/4$ compound. In contrast, the $x = 1/3$ member has frustration due to the triangular Fe lattice and a much softer coercive field.[5,25] Figure 5a displays a close-up view of the Raman response of $Fe_{1/4}TaS_2$ at three characteristic temperatures. The rattling excitations become sharper and more well-separated with decreasing temperature due to standard mode hardening and line width effects. The in-plane excitation hardens most noticeably, at roughly twice the rate of the out-of-plane mode. We also observe a TaS_2 layer twisting mode nearby at 110 cm^{-1}, which softens at low temperatures. This effect is probably associated with a weak interlayer interaction between the Fe monolayer and TaS_2 slab.

Figure 5b,c displays frequency vs temperature for the in- and out-of-plane modes of the intercalated Fe monolayer in $Fe_{1/4}TaS_2$. We use a Boltzmann sigmoid model to capture anharmonic and short-range interactions.[51,52] The spectral data deviate from the fit below the 160 K ferromagnetic ordering temperature. The strong frequency shift across a magnetic ordering transition is clear evidence for spin-phonon coupling.[53−55] Assuming only nearest neighbor exchange interactions in the Fe monolayer (probably interacting through the S centers on the chalcogenide slabs), we extract the spin-phonon coupling constant as[53,56]

$$\omega = \omega_0 + \lambda\langle S_i \cdot S_j \rangle \tag{3}$$

Here, ω_0 denotes the unperturbed phonon frequency, ω is the renormalized frequency in the presence of spin-phonon coupling, $\langle S_i \cdot S_j \rangle$ is the spin−spin correlation function, and λ is the spin-phonon coupling constant. To extract the coupling constant, we assume a limiting low-temperature value of the spin−spin correlation function: $\langle S_i \cdot S_j \rangle = S^2 = (2)^2 = 4$. We find λ values for the in- and out-of-plane excitations to be 1.1 and 0.3 cm^{-1}, respectively. In-plane coupling is thus an order of magnitude larger than the out-of-plane effect. Spin-phonon coupling constants for other vibrational modes in $Fe_{1/4}TaS_2$ are summarized in Table S1, Supporting Information.

How Do Metal Monolayer Excitations Influence Properties? It is well-known that rattlers in filled cavities and channels impact thermoelectricity and ionic conductivity.[50,57−59] In this context, a rattler consists of a weakly bound atom with a large thermal ellipsoid confined to a cavity or cage. Our situation is different because metal monolayer excitations are coherent, and as a result, they can change properties in completely different ways. In fact, any mechanism requiring a highly polarizable response or peak in the dielectric constant can benefit from these excitations. Because the collective excitations of intercalated metal monolayers act as highly sensitive terahertz resonators, this work may open opportunities for ultra-fine sensing and flash LiDAR detection. That the in-plane mode is more intense than the majority of chalcogenide slab-related phonons is useful for these applications.

Our structure−property relations suggest that external stimuli can tune metal monolayer excitations. One such example is electrical switching in $Fe_{1/3}NbS_2$, another magnetically intercalated transition metal dichalcogenide of interest as an antiferromagnetic spintronic device.[5] Here, the current draws the Fe centers back and forth, supported by the facile in-plane motion of the Fe network that we discuss in this work. Switching occurs as the field-induced motion of the ions changes both the low-temperature magnetism and transport properties. The ability to use a current pulse to rotate an in-plane component of the antiferromagnetic order[5] is also interesting and potentially related to the ability of the $x = 1/3$ materials to support chiral phonons.[60]

Metal monolayer excitations may even influence crystal growth and microstructure. For instance, the structural Z_6 vortices in chiral $Co_{1/3}NbS_2$ and $Cr_{1/3}TaS_2$ are associated with antiphase domains with in-plane shift of intercalants, and the formation of Z_6 vortices[61] likely results from an order−disorder transition of intercalants far above room temperature. The in-plane monolayer excitations may act as a soft mode for this type of transition.

SUMMARY AND OUTLOOK

We combined Raman scattering spectroscopy with complementary lattice dynamics calculations to uncover the fundamental excitations of intercalated metal monolayers in the Fe_xTaS_2 ($x = 0$, 1/4, and 1/3) family of materials. Extension to related systems including Cr_xNbS_2 ($x = 0$, 1/3) and $RbFe(SO_4)_2$ reveals similar features that we describe as in- and out-of-plane excitations of the embedded metal monolayers. We discuss the frequency, lifetime, and intensity trends as well as a spin-phonon coupling in terms of the in-plane metal−metal distance, the size of the van der Waals gap, and the mass ratio between the intercalant and the chalcogenide slab. These structure−property relations along with our model for frequency vs mass ratio effects suggest that external stimuli such as pressure and strain may be able to tune these excitations. We discuss the consequences for properties including thermoelectricity and electrical switching in antiferromagnetic spintronic devices as well as processes such as phase transition mechanisms and domain formation.

METHODS

Single Crystal Growth and Characterization. 2H−Fe_xTaS_2 ($x = 0$, 1/4, and 1/3), 2H−Cr_xNbS_2 ($x = 0$, 1/3, and $RbFe(SO_4)_2$ were grown using chemical vapor transport techniques and hydrothermal methods.[25,27,38,62] The Fe/Cr concentrations were confirmed using energy dispersive X-ray spectroscopy, magnetization, and TEM (electron diffraction + dark field images (Figure S1)).[25,27,63] Basic characterization, including TEM evidence for chirality in $Fe_{1/3}TaS_2$, is shown in refs 25 and 27. The Supporting Information contains additional details.

Raman Scattering Spectroscopy. Raman scattering measurements (λ_{excit} = 476, 532 nm; ≤3.2 mW; averaged 45 s integrations; 4.2−300 K) were performed in the back-scattering geometry using a Labram HR Evolution spectrometer. An open flow cryostat provided temperature control.

Lattice Dynamics Calculations. Phonon calculations employed density functional theory provided with QuantumATK.[64−66] Using a local density approximation on 3 × 3 × 3 unit cell repetitions, we examined phonon density of states and vibrational modes for comparison with and assignment of the experimental features. For dynamical matrix calculations, we used 3 × 3 × 3 repetitions of the various unit cells, which produced supercells consisting of 27 unit cells with a total of 162 to 702 atoms depending on the system. Details are available in Supporting information.

https://dx.doi.org/10.1021/acs.nanolett.0c03292
Nano Lett. 2021, 21, 99−106

■ ASSOCIATED CONTENT

Supporting Information

The Supporting Information is available free of charge at https://pubs.acs.org/doi/10.1021/acs.nanolett.0c03292.

Details of the density functional calculations, phonon density of states, phonon assignments, effect of the mass ratio on intercalated mode frequencies, crystal growth details, temperature dependence of the parent compound and the intercalated analogues, analysis of phonon lifetimes, and an analysis of spin-phonon coupling in $Fe_{1/3}TaS_2$ and $Cr_{1/3}NbS_2$ (PDF)

Animation of the out-of-plane, out-of-phase phonon mode for the $Fe_{1/3}TaS_2$ compound (GIF)

Animation of the in-plane, out-of-phase phonon mode for the $Fe_{1/4}TaS_2$ compound (GIF)

Animation of the out-of-plane, out-of-phase phonon mode for the $Fe_{1/4}TaS_2$ compound (GIF)

Animation of the in-plane, out-of-phase phonon mode for the $Fe_{1/3}TaS_2$ compound (GIF)

■ AUTHOR INFORMATION

Corresponding Author

Janice L. Musfeldt − *Department of Chemistry and Department of Physics and Astronomy, University of Tennessee, Knoxville, Tennessee 37996, United States;* orcid.org/0000-0002-6241-823X; Email: musfeldt@utk.edu

Authors

Shiyu Fan − *Department of Physics and Astronomy, University of Tennessee, Knoxville, Tennessee 37996, United States;* orcid.org/0000-0002-7857-0148

Sabine Neal − *Department of Chemistry, University of Tennessee, Knoxville, Tennessee 37996, United States*

Choongjae Won − *Laboratory for Pohang Emergent Materials and Max Plank POSTECH Center for Complex Phase Materials, Pohang University of Science and Technology, Pohang 790-784, Korea*

Jaewook Kim − *Rutgers Center for Emergent Materials and Department of Physics and Astronomy, Rutgers University, Piscataway, New Jersey 08854, United States; Korea Atomic Energy Research Institute, Daejeon 34057, Republic of Korea*

Deepak Sapkota − *Department of Physics and Astronomy, University of Tennessee, Knoxville, Tennessee 37996, United States*

Feiting Huang − *Department of Physics and Astronomy and Rutgers Center for Emergent Materials, Rutgers University, Piscataway, New Jersey 08854, United States*

Junjie Yang − *Department of Physics, New Jersey Institute of Technology, Newark, New Jersey 07102, United States*

David G. Mandrus − *Department of Materials Science and Engineering, The University of Tennessee, Knoxville, Tennessee 37996, United States; Materials Science and Technology Division, Oak Ridge National Laboratory, Oak Ridge, Tennessee 37831, United States*

Sang-Wook Cheong − *Department of Physics and Astronomy and Rutgers Center for Emergent Materials, Rutgers University, Piscataway, New Jersey 08854, United States; Laboratory for Pohang Emergent Materials and Max Plank POSTECH Center for Complex Phase Materials, Pohang University of Science and Technology, Pohang 790-784, Korea*

Jason T. Haraldsen − *Department of Physics, University of North Florida, Jacksonville, Florida 32224, United States;* orcid.org/0000-0002-8641-5412

Complete contact information is available at: https://pubs.acs.org/10.1021/acs.nanolett.0c03292

Author Contributions

This project was conceived by J.L.M. and S.F. The Fe_xTaS_2 (x = 1/4 and 1/3) single crystals were grown by C.J.W. and J.W.K. with advice from S.W.C., and the $Cr_{1/3}NbS_2$ single crystal was grown by S.D. with advice from DGM. $RbFe(SO_4)_2$ single crystals were grown by J.Y. Raman scattering measurements were performed by S.F. and S.N.N., and data were analyzed by S.F., S.N.N., and J.L.M. Theoretical analysis and density functional calculations were carried out by J.T.H. TEM measurements were performed by F.T.H. All authors discussed the data. The manuscript was written by S.F., S.N.N., J.T.H., and J.L.M. All authors read the paper and commented on the manuscript.

Notes

The authors declare no competing financial interest.

■ ACKNOWLEDGMENTS

Research at the University of Tennessee is supported by the U.S. Department of Energy, Office of Basic Energy Sciences, Materials Science Division under Award DE-FG02-01ER45885. J.T.H. acknowledges funding from the Institute for Materials Science at Los Alamos National Laboratory. Work at Rutgers is supported by the NSF-DMREF program (DMR-1629059). Research at Postech is supported by the National Research Foundation of Korea (NRF) funded by the Ministry of Science and ICT (Grant 2016K1A4A4A01922028). D.G.M. acknowledges research funding from the Gordon and Betty Moore Foundation's EPiQS Initiative, Grant GBMF9069. We thank A. V. Balatsky and D. H. Vanderbilt for useful discussions.

■ REFERENCES

(1) Rhead, G. E. Metal monolayers. *Contemp. Phys.* **1983**, *24*, 535.

(2) Chen, W.; Santos, E. J. G.; Zhu, W.; Kaxiras, E.; Zhang, Z. Tuning the electronic and chemical properties of monolayer MoS_2 adsorbed on transition metal substrates. *Nano Lett.* **2013**, *13*, 509.

(3) Bogicevic, A.; Jennison, D. R. Variations in the nature of metal adsorption on ultrathin Al_2O_3 films. *Phys. Rev. Lett.* **1999**, *82*, 4050.

(4) Luo, L.; Zhao, B.; Xiang, B.; Wang, C.-M. Size-controlled intercalation-to-conversiontransition in lithiation of transition-metal chalcogenides-$NbSe_3$. *ACS Nano* **2016**, *10*, 1249.

(5) Nair, N. L.; Maniv, E.; John, C.; Doyle, S.; Orenstein, J.; Analytis, J. G. Electrical switching in a magnetically intercalated transition metal dichalcogenide. *Nat. Mater.* **2020**, *19*, 153.

(6) Nakamura, K.; Shimabukuro, R.; Fujiwara, Y.; Akiyama, T.; Ito, T.; Freeman, A. J. Giant modification of the magnetocrystalline anisotropy in transition-metal monolayers by an external electric field. *Phys. Rev. Lett.* **2009**, *102*, 187201.

(7) Zheng, S.; So, J.-K.; Liu, F.; Liu, Z.; Zheludev, N.; Fan, H. J. Giant enhancement of cathodoluminescence of monolayer transitional metal dichalcogenides semiconductors. *Nano Lett.* **2017**, *17*, 6475.

(8) Wang, Y.; Li, L.; Yao, W.; Song, S.; Sun, J. T.; Pan, J.; Ren, X.; Li, C.; Okunishi, E.; Wang, Y.-Q.; Wang, E.; Shao, Y.; Zhang, Y. Y.; Yang, H.-T.; Schwier, E. F.; Iwasawa, H.; Shimada, K.; Taniguchi, M.; Cheng, Z.; Zhou, S.; Du, S.; Pennycook, S. J.; Pantelides, S. T.; Gao, H.-J. Monolayer $PtSe_2$, a new semiconducting transition-metal-

dichalcogenide, epitaxially grown by direct selenization of Pt. *Nano Lett.* **2015**, *15*, 4013.
(9) Yu, Y.; Li, G.; Huang, L.; Barrette, A.; Cai, Y.-Q.; Yu, Y. L.; Gundogdu, K.; Zhang, Y.-W.; Cao, L. Enhancing multifunctionalities of transition-metal dichalcogenide monolayers via cation intercalation. *ACS Nano* **2017**, *11*, 9390.
(10) Dresselhaus, M. S.; Dresselhaus, G. Intercalation compounds of graphite. *Adv. Phys.* **1981**, *30*, 139.
(11) Weller, T. E.; Ellerby, M.; Saxena, S. S.; Smith, R. P.; Skipper, N. T. Superconductivity in the intercalated graphite compounds C_6Yb and C_6Ca. *Nat. Phys.* **2005**, *1*, 39−41.
(12) Tiwari, A. P.; Shin, S.; Hwang, E.; Jung, S.-G.; Park, T.; Lee, H. Superconductivity at 7.4 K in few layer graphene by Li-intercalation. *J. Phys.: Condens. Matter* **2017**, *29*, 445701.
(13) Ichinokura, S.; Sugawara, K.; Takayama, A.; Takahashi, T.; Hasegawa, S. Superconducting calcium-intercalated bilayer graphene. *ACS Nano* **2016**, *10*, 2761.
(14) Margine, E. R.; Lambert, H.; Giustino, F. Electron-phonon interaction and pairing mechanism insuperconducting Ca-intercalated bilayer graphene. *Sci. Rep.* **2016**, *6*, 21414.
(15) Eames, C.; Islam, M. S. Ion intercalation into two-dimensional transition-metal carbides: globalscreening for new high-capacity battery materials. *J. Am. Chem. Soc.* **2014**, *136*, 16270.
(16) Wang, X.; Shen, X.; Wang, Z.; Yu, R.; Chen, L. Atomic-scale clarification of structural transition of MoS_2 upon sodium intercalation. *ACS Nano* **2014**, *8*, 11394.
(17) Kumar, P.; Skomski, R.; Pushpa, R. Magnetically ordered transition-metal-intercalated WSe_2. *ACS Omega.* **2017**, *2*, 7985.
(18) Togawa, Y.; Koyama, T.; Takayanagi, K.; Mori, S.; Kousaka, Y.; Akimitsu, J.; Nishihara, S.; Inoue, K.; Ovchinnikov, A. S.; Kishine, J. Chiral magnetic soliton lattice on a chiral helimagnet. *Phys. Rev. Lett.* **2012**, *108*, 107202.
(19) Morosan, E.; Zandbergen, H. W.; Li, L.; Lee, M.; Checkelsky, J. G.; Heinrich, M.; Siegrist, T.; Ong, N. P.; Cava, R. J. Sharp switching of the magnetization in $Fe_{1/4}TaS_2$. *Phys. Rev. B: Condens. Matter Mater. Phys.* **2007**, *75*, 104401.
(20) Fan, S.; Manuel, I.; al-Wahish, A.; O'Neal, K. R.; Smith, K. A.; Won, C. J.; Kim, J. W.; Cheong, S.-W.; Haraldsen, J. T.; Musfeldt, J. L. Electronic chirality in the metallic ferromagnet $Fe_{1/3}TaS_2$. *Phys. Rev. B: Condens. Matter Mater. Phys.* **2017**, *96*, 205119.
(21) Hu, W. Z.; Li, G.; Yan, J.; Wen, H. H.; Wu, G.; Chen, X. H.; Wang, N. L. Optical study of the charge-density-wave mechanism in 2H-TaS_2 and Na_xTaS_2. *Phys. Rev. B: Condens. Matter Mater. Phys.* **2007**, *76*, No. 045103.
(22) Morosan, E.; Zandbergen, H. W.; Dennis, B. S.; Bos, J. W. G.; Onose, Y.; Klimczuk, T.; Ramirez, A. P.; Ong, N.P.; Cava, R. J. Superconductivity in Cu_xTiSe_2. *Nat. Phys.* **2006**, *2*, 544.
(23) Heguri, S.; Kawade, N.; Fujisawa, T.; Yamaguchi, A.; Sumiyama, A.; Tanigaki, K.; Kobayashi, M. Superconductivity in the graphite intercalation compound BaC_6. *Phys. Rev. Lett.* **2015**, *114*, 247201.
(24) Li, L. J.; Lu, W. J.; Zhu, X. D.; Ling, L. S.; Qu, Z.; Sun, Y. P. Fe-doping−induced superconductivity in the charge-density-wave system 1T-TaS_2. *EPL* **2012**, *97*, 67005.
(25) Horibe, Y.; Yang, J.; Cho, Y. H.; Luo, X.; Kim, S. B.; Oh, Y. S.; Huang, F. T.; Asada, T.; Tanimura, M.; Jeong, D.; Cheong, S.-W. Color theorems, chiral domain topology, and magnetic properties of Fe_xTaS_2. *J. Am. Chem. Soc.* **2014**, *136*, 8368.
(26) Meetsma, A.; Wiegers, G. A.; Haange, R. J.; de Boer, J. L. Structure of 2H-TaS_2. *Acta Crystallogr., Sect. C: Cryst. Struct. Commun.* **1990**, *46*, 1598.
(27) Ghimire, N. J.; McGuire, M. A.; Parker, D. S.; Sipos, B.; Tang, S.; Yan, J.-Q.; Sales, B. C.; Mandrus, D. Magnetic phase transition in single crystals of the chiral helimagnet $Cr_{1/3}NbS_2$. *Phys. Rev. B: Condens. Matter Mater. Phys.* **2013**, *87*, 104403.
(28) Serrano-González, H.; Bramwell, S. T.; Harris, K. D. M.; Kariuki, B. M.; Nixon, L.; Parkin, I. P.; Ritter, C. Magnetic structures of the triangular lattice magnets $AFe(SO_4)_2$ (A=K, Rb, Cs). *J. Appl. Phys.* **1998**, *83*, 6314.
(29) Mankovsky, S.; Chadova, K.; Kodderitzsch, D.; Minar, J.; Ebert, H.; Bensch, W. Electronic, magnetic, and transport properties of Fe-intercalated 2H-TaS_2 studied by means of the KKR-CPA method. *Phys. Rev. B: Condens. Matter Mater. Phys.* **2015**, *92*, 144413.
(30) Dijkstra, J.; Zijlema, P. J.; van Bruggen, C. F.; Haas, C.; and de Groot, R. A. Band-structure calculations of $Fe_{1/3}TaS_2$ and $Mn_{1/3}TaS_2$, and transport and magnetic properties of $Fe_{0.28}TaS_2$. *J. Phys.: Condens. Matter* **1989**, *1*, 6363.
(31) Mattheiss, L. F. Band structures of transition-metal-dichalcogenide layer compounds. *Phys. Rev. B* **1973**, *8*, 3719.
(32) Barath, H.; Kim, M.; Karpus, J. F.; Cooper, S. L.; Abbamonte, P.; Fradkin, E.; Morosan, E.; Cava, R.J. Quantum and classical mode softening near the charge density wave-superconductor transition in Cu_xTiSe_2. *Phys. Rev. Lett.* **2008**, *100*, 106402.
(33) Togawa, Y.; Kishine, J.; Nosov, P. A.; Koyama, T.; Paterson, G. W.; McVitie, S.; Kousaka, Y.; Akimitsu, J.; Ogata, M.; Ovchinnikov, A. S. Anomalous temperature behavior of the chiral spin helix in $CrNb_3S_6$ thin lamellae. *Phys. Rev. Lett.* **2019**, *122*, No. 017204.
(34) Aoki, R.; Kousaka, Y.; Togawa, Y. Anomalous nonreciprocal electrical transport on chiralmagnetic order. *Phys. Rev. Lett.* **2019**, *122*, No. 057206.
(35) Tang, S.; Fishman, R. S.; Okamoto, S.; Yi, J.; Zou, Q.; Fu, M.; Li, A.; Mandrus, D.; Gai, Z. Tuning magnetic soliton phase via dimensional confinement in exfoliated 2D $Cr_{1/3}NbS_2$ thin flakes. *Nano Lett.* **2018**, *18*, 4023.
(36) Wang, L.; Chepiga, N.; Ki, D.-K.; Li, L.; Li, F.; Zhu, W.; Kato, Y.; Ovchinnikova, O. S.; Mila, F.; Martin, I.; Mandrus, D.; Morpurgo, A. F. Controlling the topological sector of magnetic solitons in exfoliated $Cr_{1/3}NbS_2$ Crystals. *Phys. Rev. Lett.* **2017**, *118*, 257203.
(37) Clements, E. M.; Das, R.; Phan, M.-H.; Li, L.; Keppens, V.; Mandrus, D.; Osofsky, M.; Srikanth, H. Magnetic field dependence of nonlinear magnetic response and tricritical point in the monoaxial chiral helimagnet $Cr_{1/3}NbS_2$. *Phys. Rev. B: Condens. Matter Mater. Phys.* **2018**, *97*, 214438.
(38) Yang, J., et al. In preparation, 2020.
(39) Klimin, S. A.; Popova, M. N.; Mavrin, B. N.; van Loosdrecht, P. H. M.; Svistov, L. E.; Smirnov, A. I.; Prozorova, L. A.; von Nidda, H.-A. K.; Seidov, Z.; Loidl, A.; Shapiro, A. Y.; Demianets, L. N. Structural phase transition in the two-dimensional triangular lattice antiferromagnet $RbFe(MoO_4)_2$. *Phys. Rev. B: Condens. Matter Mater. Phys.* **2003**, *68*, 174408.
(40) Zhang, X.; Qiao, X.; Shi, W.; Wu, J.; Jiang, D.; Tan, P. Phonon and Raman scattering of two-dimensional transition metal dichalcogenides from monolayer, multilayer to bulk material. *Chem. Soc. Rev.* **2015**, *44*, 2757.
(41) Sugai, S.; Murase, K.; Uchida, S.; Tanaka, S. Studies of lattice dynamics in 2H-TaS_2 by Raman scattering. *Solid State Commun.* **1981**, *40*, 399.
(42) McMullan, W. G.; Irwin, J. C. Long-wavelength phonons in 2H−NbS_2, 2H−TaS_2, and Ag_xTaS_2. *Can. J. Phys.* **1984**, *62*, 789.
(43) Shi, J.; Wang, X.; Zhang, S.; Xiao, L.; Huan, Y.; Gong, Y.; Zhang, Z.; Li, Y.; Zhou, X.; Hong, M.; Fang, Q.; Zhang, Q.; Liu, X.; Gu, L.; Liu, Z.; Zhang, Y. Two-dimensional metallic tantalum disulfide as ahydrogen evolution catalyst. *Nat. Commun.* **2017**, *8*, 958.
(44) Joshi, J.; Hill, H. M.; Chowdhury, S.; Malliakas, C. D.; Tavazza, F.; Chatterjee, U.; Hight Walker, A. R.; Vora, P. M. Short-range charge density wave order in 2H-TaS_2. *Phys. Rev. B: Condens. Matter Mater. Phys.* **2019**, *99*, 245144.
(45) Hajiyev, P.; Cong, C.; Qiu, C.; Yu, T. Contrast and Raman spectroscopy study of single- and few-layered charge density wave material: 2H-$TaSe_2$. *Sci. Rep.* **2013**, *3*, 2593.
(46) Guillamón, I.; Suderow, H.; Vieira, S.; Cario, L.; Diener, P.; Rodière, P. Superconducting density of states and vortex cores of 2H-NbS_2. *Phys. Rev. Lett.* **2008**, *101*, 166407.
(47) Kacmarcik, J.; Pribulova, Z.; Marcenat, C.; Klein, T.; Rodiere, P.; Cario, L.; Samuely, P. Specific heat measurements of a superconducting NbS_2 single crystal in an external magnetic field: energy gap structure. *Phys. Rev. B: Condens. Matter Mater. Phys.* **2010**, *82*, No. 014518.

https://dx.doi.org/10.1021/acs.nanolett.0c03292
Nano Lett. 2021, 21, 99−106

(48) Moncton, D. E.; Axe, J. D.; DiSalvo, F. J. Study of superlattice formation in 2H-$NbSe_2$ and 2H-$TaSe_2$ by neutron scattering. *Phys. Rev. Lett.* **1975**, *34*, 734.
(49) Tissen, V. G.; Osorio, M. R.; Brison, J. P.; Nemes, N. M.; García-Hernández, M.; Cario, L.; Rodière, P.; Vieira, S.; Suderow, H. Pressure dependence of superconducting critical temperature and upper critical field of 2H-NbS_2. *Phys. Rev. B: Condens. Matter Mater. Phys.* **2013**, *87*, 134502.
(50) Voneshen, D. J.; Refson, K.; Borissenko, E.; Krisch, M.; Bosak, A.; Piovano, A.; Cemal, E.; Enderle, M.; Gutmann, M. J.; Hoesch, M.; Roger, M.; Gannon, L.; Boothroyd, A. T.; Uthayakumar, S.; Porter, D. G.; Goff, J.P. Suppression of thermal conductivity by rattling modes in thermoelectric sodium cobaltate. *Nat. Mater.* **2013**, *12*, 1028.
(51) Yokosuk, M. O.; Artyukhin, S.; al-Wahish, A. B.; Wang, X.; Yang, J.; Li, Z.; Cheong, S.-W.; Vanderbilt, D.; Musfeldt, J. L. Tracking the continuous spin-flop transition in Ni_3TeO_6 by infrared spectroscopy. *Phys. Rev. B: Condens. Matter Mater. Phys.* **2015**, *92*, 144305.
(52) Casto, L. D.; Clune, A. J.; Yokosuk, M. O.; Musfeldt, J. L.; Williams, T. J.; Zhuang, H. L.; Lin, M.-W.; Xiao, K.; Hennig, R. G.; Sales, B. C.; Yan, J.-Q.; Mandrus, D. Strong spin-lattice coupling in $CrSiTe_3$. *APL Mater.* **2015**, *3*, No. 041515.
(53) Rudolf, T.; Kant, C.; Mayr, F.; Hemberger, J.; Tsurkan, V.; Loidl, A. Polar phonons and spin-phonon coupling in $HgCr_2S_4$ and $CdCr_2S_4$, studied with far-infrared spectroscopy. *Phys. Rev. B: Condens. Matter Mater. Phys.* **2007**, *76*, 174307.
(54) Wysocki, A. L.; Birol, T. Magnetically induced phonon splitting in ACr_2O_4 spinels from first principles. *Phys. Rev. B: Condens. Matter Mater. Phys.* **2016**, *93*, 134425.
(55) Sushkov, A. B.; Tchernyshyov, O.; Ratcliff, W.; Cheong, S.-W.; Drew, H. D. Probing spin correlations with phonons in the strongly frustrated magnet $ZnCr_2O_4$. *Phys. Rev. Lett.* **2005**, *94*, 137202.
(56) Fennie, C. J.; Rabe, K. M. Magnetically induced phonon anisotropy in $ZnCr_2O_4$ from first principles. *Phys. Rev. Lett.* **2006**, *96*, 205505.
(57) Mandrus, D.; Sales, B. C.; Jin, R. Localized vibrational mode analysis of the resistivity and specific heat of LaB_6. *Phys. Rev. B: Condens. Matter Mater. Phys.* **2001**, *64*, No. 012302.
(58) Sales, B. C.; Mandrus, D.; Williams, R. K. Filled skutterudite antimonides: a new class of thermoelectric materials. *Science* **1996**, *272*, 1325.
(59) Choi, J.; Musfeldt, J. L.; Wang, Y. J.; Koo, H.-J.; Whangbo, M.-H.; Galy, J.; Millet, P. Optical investigation of $Na_2V_3O_7$ nanotubes. *Chem. Mater.* **2002**, *14*, 924.
(60) Zhu, H.; Yi, J.; Li, M.-Y.; Xiao, J.; Zhang, L.; Yang, C.-W.; Kaindl, R. A.; Li, L.-J.; Wang, Y.; Zhang, X. Observation of chiral phonons. *Science* **2018**, *359*, 579−582.
(61) Chae, S. C.; Horibe, Y.; Jeong, D. Y.; Rodan, S.; Lee, N.; Cheong, S.- W. Self-organization, condensation, and annihilation of topological vortices and antivortices in a multiferroic. *Proc. Natl. Acad. Sci. U. S. A.* **2010**, *107*, 21366−21370.
(62) Miyadai, T.; Kikuchi, K.; Kondo, H.; Sakka, S.; Arai, K.; Ishikawa, Y. Magnetic properties of $Cr_{1/3}NbS_2$. *J. Phys. Soc. Jpn.* **1983**, *52*, 1394.
(63) Newbury, D. E.; Ritchie, N. W. M. Is scanning electron microscopy/energy dispersive X-ray spectrometry (SEM/EDS) quantitative? *Scanning* **2013**, *35*, 141−168.
(64) *Synopsys QuantumATK. QuantumATK version 0-2018.06*. https://www.synopsys.com/silicon/quantumatk.html (accessed November 10, 2020).
(65) Smidstrup, S.; Stradi, D.; Wellendorff, J.; Khomyakov, P. A.; Vej-Hansen, U. G.; Lee, M.-E.; Ghosh, T.; Jónsson, E.; Jónsson, H.; Stokbro, K. First-principles Green's-function method for surface calculations: a pseudopotential localized basis set approach. *Phys. Rev. B: Condens. Matter Mater. Phys.* **2017**, *96*, 195309.
(66) Smidstrup, S.; Markussen, T.; Vancraeyveld, P.; Wellendorff, J.; Schneider, J.; Gunst, T.; Verstichel, B.; Stradi, D.; Khomyakov, P. A.; Vej-Hansen, U. G.; et al. Quantum ATK: an integrated platform of electronic and atomic-scale modelling tools. *J. Phys.: Condens. Matter* **2020**, *32*, No. 015901.

https://dx.doi.org/10.1021/acs.nanolett.0c03292
Nano Lett. 2021, 21, 99−106